

## Angle-resolved photoemission on untwinned $\text{YBa}_2\text{Cu}_3\text{O}_{6.95}$ . II. Determination of Fermi surfaces

Matthias C. Schabel

*Department of Applied Physics, Stanford University, Stanford, California 94305*

C.-H. Park

*Department of Applied Physics, Department of Physics, and Stanford Synchrotron Radiation Laboratory, Stanford University, Stanford, California 94305*

A. Matsuura

*Department of Applied Physics and Department of Physics, Stanford University, Stanford, California 94305*

Z.-X. Shen

*Department of Applied Physics and Stanford Synchrotron Radiation Laboratory, Stanford University, Stanford, California 94305*

D. A. Bonn, Ruixing Liang, and W. N. Hardy

*Department of Physics and Astronomy, University of British Columbia, Vancouver, British Columbia, Canada V6T 1Z1*

(Received 25 July 1997)

We present complete Fermi-surface mappings of an untwinned single crystal of  $\text{YBa}_2\text{Cu}_3\text{O}_{7-\delta}$  in two distinct photon polarization geometries. Various methods for Fermi-surface determination with angle-resolved photoelectron spectroscopy are discussed and a technique based on the momentum space density of states is developed and applied. The data reveal the presence of two  $\text{CuO}_2$  plane-derived Fermi-surface pockets, along with weak evidence for a single chain sheet, in agreement with earlier work on twinned crystals and *ab initio* predictions, but show no sign of the expected “stick” pocket centered at  $(\pi, \pi)$ . In contrast with earlier work on  $\text{Bi}_2\text{Sr}_2\text{CaCu}_2\text{O}_{8+\delta}$ , we see no evidence for “shadow bands” in optimally doped  $\text{YBa}_2\text{Cu}_3\text{O}_{7-\delta}$ , supporting the contention that these features arise from structural rather than magnetic correlations. [S0163-1829(98)04810-3]

### I. INTRODUCTION AND EXPERIMENTAL TECHNIQUE

The observation of large, bandlike Fermi surfaces in both electron- and hole-doped high- $T_c$  superconductors with angle-resolved photoemission<sup>1-5</sup> (ARPES) places strong constraints on many-body theories for these systems, and has led to extensive discussion of the Luttinger sum rule and the relevance of Fermi-liquid theory to the electronic structure of the cuprates in the metallic doping regime. Two important questions can be addressed by Fermi-surface (FS) measurements on two-layer cuprates: (i) do two FS pockets arising from coupling of the  $\text{CuO}_2$  bilayers exist? and (ii) do “shadow bands” originating in antiferromagnetic (AF) correlations appear as echoes of the Fermi surface shifted by the AF wave vector,  $(\pi, \pi)$ ? To adequately analyze these issues, it is essential to understand what is being measured in an ARPES experiment, how a FS is defined in a many-body correlated system which may be far from the Fermi-liquid ideal, and how that information is extracted from the experimental data. In this paper we discuss various methods for extraction of Fermi surfaces from ARPES data,<sup>6-9</sup> discuss the implementation and relative merits of these, present a complete Fermi-surface mapping of an untwinned single crystal of  $\text{YBa}_2\text{Cu}_3\text{O}_{7-\delta}$  (Y123) for two distinct polarization geometries, and compare the results with both local-density approximation (LDA) predictions and measurements on other high- $T_c$  superconductors.

In  $\text{Bi}_2\text{Sr}_2\text{CaCu}_2\text{O}_{8+\delta}$  (Bi2212), complications arising from superstructure have led to contradictory conclusions regarding the presence or absence of bilayer splitting, despite similar data,<sup>5,10</sup> highlighting the subjectivity of conventional FS attribution. Because the predicted magnitude of the splitting in Bi2212 is much smaller than that for optimally doped Y123, the latter material is much more appropriate for such investigations. In addition, Y123 does not suffer from the Bi2212 superstructure distortion, although its FS is complicated by the presence of four distinct segments and significant  $k_z$  dispersion, based on predictions of *ab initio* local-density approximation (LDA) calculations.<sup>11-13</sup> Also important is the fact that no complete FS mapping has been performed on an untwinned sample,<sup>14</sup> even though twinning renders interpretation of the data more difficult. Significant anisotropy is predicted in the band structure and FS of Y123 due to the  $\text{CuO}_3$  chains breaking the fourfold tetragonal symmetry. This leads to smearing of the spectral functions and FS of twinned crystals by superimposition of the  $\Gamma X \Sigma \Gamma$  and  $\Gamma Y \Sigma \Gamma$  octants of the Brillouin zone.

Interest in the possibility of directly observing strong antiferromagnetic correlation effects in the Fermi surface of the cuprates<sup>3</sup> was brought to the forefront by Aebi’s report<sup>7,15</sup> of antiferromagnetic “shadow bands” in data taken in photoelectron diffraction mode on optimally doped Bi2212 in the normal state at room temperature. Such a dramatic manifestation of magnetic behavior in a doping and temperature regime where the antiferromagnetic correlation lengths are of

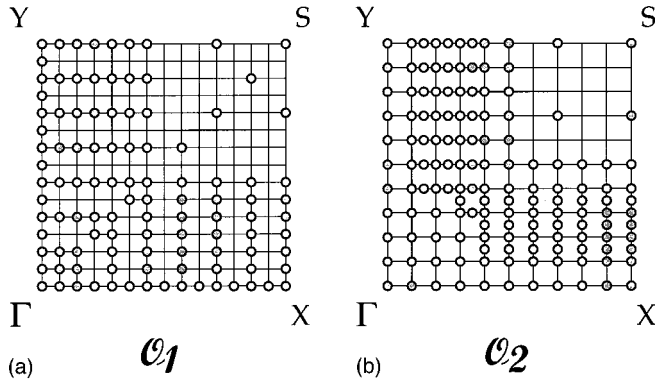


FIG. 1. The  $\mathbf{k}$ -space grids over which ARPES spectra were acquired. Each point represents a full photoemission EDC covering an energy window of approximately 1 eV below the Fermi energy.  $\mathcal{O}_1$  (a) corresponds to photon polarization parallel to  $\Gamma S$ ;  $\mathcal{O}_2$  (b) to polarization parallel to  $\Gamma Y$ .

the order of a planar lattice constant, at most, would have strong implications for the relevance of magnetically mediated pairing in the microscopic mechanism for superconductivity. Unfortunately, the possibility of a  $c(2 \times 2)$  reconstruction in Bi2212 and other experimental difficulties hinders discrimination of such correlations from simple structural effects.<sup>16,17</sup> The absence of these uncertainties in Y123, as well as a much better understanding of the details of the crystal structure, makes Y123 potentially better suited to address these questions as well.

Our experimental setup and apparatus are discussed extensively in the preceding paper;<sup>18</sup> only relevant details are reiterated here. Photoelectron energy distribution curves (EDC's) of the near  $E_F$  region were obtained over one quadrant of the two-dimensional Brillouin zone (BZ) in two distinct sample orientations, one with the plane of photon polarization,  $\mathbf{E}$ , parallel to  $\Gamma S$  [(0,0)–( $\pi$ , $\pi$ )] (denoted  $\mathcal{O}_1$ ) and the other parallel to  $\Gamma Y$  [(0,0)–(0, $\pi$ )] (denoted  $\mathcal{O}_2$ ). Figures 1(a) and 1(b) show the  $\mathbf{k}$ -space grids over which EDC's were taken for each orientation. All spectra were acquired using plane polarized synchrotron radiation of  $h\nu = 28$  eV, provided by the undulator at beamline V of the Stanford Synchrotron Radiation Laboratory (SSRL). Total energy resolution was approximately 50 meV, with an angular acceptance of  $\pm 1^\circ$  corresponding to roughly 2.5% of the full BZ width. Untwinned Y123 single crystals of exceptional quality, with typical transition widths of 0.25 K, were cleaved at low-temperature parallel to the  $ab$  plane, and were maintained at or below 20 K at all times to avoid sample degradation. Chamber pressure was better than  $5 \times 10^{-11}$  torr throughout data acquisition; no noticeable changes in the spectra were observed over the course of the measurement. To compensate for fluctuations in count rates from changes in beam intensity and sample position, all spectra were normalized to the integrated photoemission weight well above the Fermi energy arising from inelastically scattered electrons excited by higher-order light.

## II. METHODS FOR FERMISURFACE DETERMINATION WITH ARPES

Conventional ARPES FS determinations infer crossings from cuts through the BZ, subjectively identifying dispersive

quasiparticles “by eye” in the EDC's. While it is impossible to attribute specific, quantitative criteria to human judgment, there are a number of guidelines which are useful in identification of crossing points. First, the centroid of the quasiparticle peak can be tracked in  $\mathbf{k}$  space and extrapolated to its intersection with the Fermi energy, this point defining the Fermi-surface boundary. Second, the total area beneath the quasiparticle peak can be monitored, with the crossing roughly corresponding to the point where this area has diminished by a factor of 2. Finally, the energy position of the midpoint of the leading edge of the EDC's may be observed, with the crossing found at the point where this quantity reaches its maximum value. Depending on the particular preferences of the practitioner, one of these methods may be strictly adhered to or some synthesis of all three may be used. In either case, the subjective method is adequate for sketching out rough details of Fermi-surface topology and for gaining a qualitative overview, but is neither quantitative nor unique, and cannot provide an unbiased, automatic means of extracting FS contours.

An alternative technique, based on photoelectron diffraction methods,<sup>6</sup> has been used by Aebi *et al.*, to measure the Fermi surface of Bi2212, among other materials.<sup>7,15,19,20</sup> In this approach, the total photoemission intensity in a narrow energy window centered on  $E_F$  is measured as a function of  $\mathbf{k}$  by scanning over the Brillouin zone. By acquiring a single data point rather than a complete EDC for each  $\mathbf{k}$  vector, it is possible to densely sample the entire BZ much more rapidly and completely than is feasible in conventional EDC mode. However, there are four disadvantages to this method. First, it only provides information on the relative spectral weight near  $E_F$ , but does not allow the identification of dispersive quasiparticle features or determination of the band structure. Second, matrix element effects and cross-section fluctuations may lead to sizeable variation of the total photoemission intensity in different parts of the BZ, over- or underemphasizing certain regions of  $\mathbf{k}$  space. Third, while the technique has intuitive appeal, the precise physical meaning of the quantity being measured is not well defined. The essential assumption which is made is that the spectral weight at the Fermi level has a maximum at  $\mathbf{k}_F$ ; this certainly holds in a simple Fermi-liquid model, but there is no particular reason to believe that this behavior is universal in strongly correlated systems. Fourth, in the instance of the high- $T_c$  materials, or other systems where there is an extended region of  $\mathbf{k}$  space having a high spectral density near but below the Fermi energy, the photoelectron diffraction method is unable to resolve true FS crossings from the near  $E_F$  weight, and will actually include contributions from occupied states lying within the greater of the instrument resolution,  $\sigma$ , or  $kT$ , of  $E_F$ .

A third technique, which has been proposed by Randeria *et al.*,<sup>8</sup> relies on the approximate sum rule relating the spectral function to the momentum space density of states (DOS),  $n(\mathbf{k})$ . As noted in their letter,  $n(\mathbf{k}) = \int_{-\infty}^{\infty} A(\mathbf{k}, \omega) f(\omega) d\omega$ . To see how this relates to what is measured in an ARPES experiment, note that, within the sudden approximation, a valence-band ARPES spectrum may be approximated as a sum over bands of the product of a matrix element for each band with the corresponding single band spectral function:  $I(\mathbf{k}, \omega) = \sum_n M_n(\mathbf{k}, h\nu) f(\omega) A_n(\mathbf{k}, \omega)$ . It is further con-

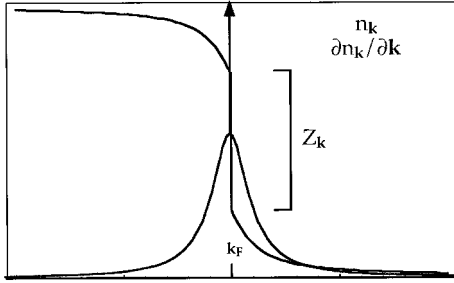


FIG. 2. A schematic illustration of the momentum space density of states,  $n(\mathbf{k})$ , and its derivative,  $[\partial n(\mathbf{k})/\partial \mathbf{k}]$  in the context of a simple Fermi-liquid model. The mass renormalization  $Z_{\mathbf{k}}$  defines the fractional quasiparticle weight in the coherent part of the spectrum.

tured that ARPES spectra may be used to directly measure  $n(\mathbf{k})$ , through the aforementioned relationship between photoemission spectra and  $A(\mathbf{k}, \omega)$ . This is true within a small region of  $\mathbf{k}$  space, if we assume that  $M_n(\mathbf{k}, h\nu)$  is weakly varying and we further restrict ourselves to a single band, in which case we can integrate over  $\omega$  to obtain  $\int_{-\Delta_n}^{\infty} I(\mathbf{k}, \omega) d\omega = M_n(\mathbf{k}, h\nu) n(\mathbf{k})$ , where  $\Delta_n$  is the quasiparticle bandwidth. Then the energy-integrated ARPES spectrum is proportional to the momentum space DOS, modulated by the photon energy and  $\mathbf{k}$  dependence of the matrix element prefactor. Unfortunately, the situation in real, multi-band materials is not nearly so simple. First, the photon energy dependence is nontrivial, and can lead to vastly different contributions from bands having different orbital character, especially in the UPS energy range. This is particularly true in structurally complex materials such as the cuprates, which have polyatomic bases with many atoms and, consequently, many overlapping bands. Second, for a global picture of the Fermi surface, the  $\mathbf{k}$  dependence of the matrix element term is likely to be significant on the scale of the Brillouin zone. In these cases, it is difficult to justify, *a priori*, straightforward application of the  $n(\mathbf{k})$  approach.

Despite these complications, it is possible to formulate a quantitative means of directly extracting Fermi-surface information from a complete set of ARPES data spanning the Brillouin zone. It is well known that, within the Fermi-liquid framework, the momentum distribution drops discontinuously at the Fermi surface, with the size of the step,  $Z_{\mathbf{k}}$ , being directly related to the mass renormalization (Fig. 2). Experimental broadening from the finite angular resolution will remove this discontinuity, leading to a sigmoid function of  $\mathbf{k}$ . In the case where multiple quasiparticles coexist, the momentum distribution will manifest several discrete drops, one for each band. If we consider the momentum space gradient of this function,  $|\nabla_{\mathbf{k}} n(\mathbf{k})|$ , it is clear that a peak will occur at the position of each Fermi surface crossing, corresponding to the steps in the momentum density. Under the assumption that the matrix element term is slowly varying relative to the characteristic “width” of the Fermi surface (primarily defined by the angular resolution of the photoemission spectrometer), the derivative of the photoemission spectral weight will manifest essentially identical behavior, allowing the Fermi surface to be directly extracted from the

data. In cases where the matrix element variation is non-negligible, a simple first-order correction may be made using the logarithmic derivative instead:  $|\nabla_{\mathbf{k}} \ln n(\mathbf{k})|$ , thereby mapping out regions where the *relative* variation in  $n(\mathbf{k})$  is large. This can be used to correct for variations in cross section due to polarization effects when data is acquired with synchrotron radiation or other polarized photon sources.

By relying on conservation of spectral weight, the presence of weight near but below  $E_F$  will not affect the appearance of the Fermi surface determined in this way, unlike the photoelectron diffraction method, nor will the finite experimental energy resolution, since the Fermi statistics defining particle conservation are unaffected by the instrumental broadening. Similarly, conservation of spectral weight is a robust property of many-body systems, independent of the details of the interactions, making this approach equally valid for strongly correlated and non-Fermi-liquid materials. An example is the Luttinger-liquid scenario, as discussed by Chakravarty *et al.*,<sup>21</sup> in which the  $\delta$  function singularity in the gradient is replaced by a power-law divergence; while the details of  $n(\mathbf{k})$  are affected, the FS crossing appears in the expected region of  $\mathbf{k}$  space. The main disadvantage of the gradient method is the fact that numerical differentiation, which magnifies the noise already present in the data, is necessary for extraction of the Fermi surface. This is particularly problematic for data taken, as ours were, in normal EDC acquisition mode, necessitating a degree of numerical smoothing for good results. The required smoothing results in slightly diminished effective  $\mathbf{k}$  resolution relative to our actual instrumental contribution. The much denser  $\mathbf{k}$  space sampling of the photoelectron diffraction measurements should allow significantly improved signal-to-noise ratio in applications of the derivative method.

In experimental implementations of the momentum space DOS methods some finite cutoff energy  $E_c$ , must be chosen over which the  $\omega$  integration is made.<sup>9</sup> Except in the ideal case where  $E_c$  lies in an energy window which is not transected by any bands from above or below, a problem due to quasiparticles appearing or disappearing through the integration limit arises, potentially leading to spurious peaks in the gradient. These false crossings may be identified in a number of ways. By examining the experimental band dispersions, it is possible to discriminate crossings of quasiparticles dispersing into or out of the window from/to lower lying states from those in which the quasiparticle actually passes through the Fermi energy. Another method is to note that the true Fermi surface is invariant with respect to the choice of  $E_c$ , so that  $(\partial/\partial E_c) \int_{E_c}^{\infty} \nabla_{\mathbf{k}} I(\mathbf{k}, \omega) d\omega = 0$ . For this reason, an important consideration in performing these experiments is the need to retain some energy distribution information, even if one is ultimately only concerned with the FS topology.

### III. THE FERMİ SURFACE OF Y123

Recently the Fribourg group has published several articles clearly demonstrating their ability to achieve significantly improved resolution of band splitting by performing ARPES studies in the photoelectron diffraction acquisition mode.<sup>19,20</sup> With this method the photoemission intensity in a fixed kinetic energy window around  $E_F$  is sampled over an ex-

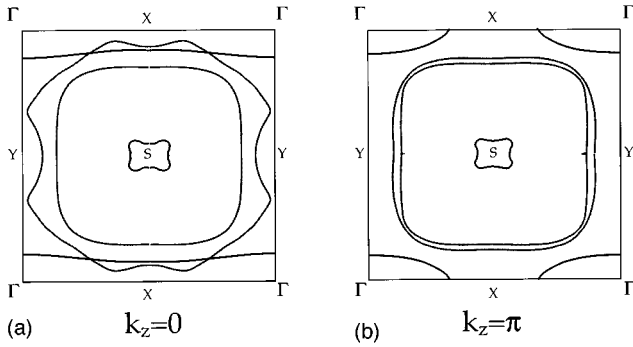


FIG. 3. Fermi surfaces calculated within the local-density approximation using the LMTO method for  $k_z=0$ , and  $k_z=\pi$ , in panels (a) and (b), respectively (Ref. 13).  $\text{CuO}_2$  plane derived sheets are shown in black, while  $\text{CuO}_3$  chain sheets are shown in gray. Unlike Bi2212, which is predicted to have very little  $c$ -axis band dispersion, the presence of  $\text{CuO}_3$  chains in Y123 leads to significant three-dimensionality, as manifested in the notable dispersion of the Fermi surfaces along  $k_z$ .

tremely fine mesh in  $\mathbf{k}$  space, complementing the normal ARPES technique of sampling EDC's over a wide energy window but at only a few points in the Brillouin zone. For purposes of comparison, we have applied this analytical approach to our data on untwinned Y123. While our data were acquired in conventional EDC mode, they constitute a comparatively dense mesh in  $\mathbf{k}$  space which we may numerically interpolate to simulate the photoelectron diffraction approach.

The Fermi surface of optimally doped Y123, calculated using the full-potential linear muffin-tin orbital (FP-LMTO) method is shown in Figs. 3(a) and 3(b) for  $k_z=0, \pi$ .<sup>12,13</sup> As studies on twinned Y123 and numerous other cuprates have made clear,<sup>3-5</sup> band-theory predictions are at least qualitatively correct for these materials, provide the only *ab initio* theoretical predictions for comparison with the experimental

data, and constitute a useful framework within which to discuss possible deviations from conventional behavior. On this basis, in the following we consistently compare our results to the LDA predictions.<sup>11-13</sup> The principal features of the LMTO Fermi surface are two large  $\text{CuO}_2$  plane-derived hole pockets centered on the  $S$  point, a chain derived FS sheet running roughly parallel to  $\Gamma X$ , and a small pocket centered on  $S$ . Projection of the orbital character of the relevant bands reveals that the inner plane pocket is principally derived from the bonding  $pd\sigma$  plane states comprised of  $\text{Cu}(2) 3d_{x^2-y^2}$ ,  $\text{O}(2) 2p_x$ , and  $\text{O}(3) 2p_y$  orbitals, while the more dispersive outer pocket derives from the corresponding antibonding  $pd\sigma^*$  states. The small “stick” pocket at  $S$  arises primarily from bonding between the apical oxygen  $\text{O}(4)$  and  $\text{Ba}$ , while the remaining  $pd\sigma$  chain sheet weakly hybridizes with the bonding  $pd\sigma$  band at  $k_z=0$  and strongly hybridizes with the antibonding  $pd\sigma^*$  band at  $k_z=\pi$ , resulting in substantial  $c$ -axis dispersion.<sup>13</sup>

Figures 4(a) and 4(b) show the photoemission intensity maps for our data at  $\omega=E_F$ , reflected along symmetry lines to span the full BZ, for both sample geometries. These plots were generated by interpolation of data taken at  $\mathbf{k}$  points shown in Figs. 1(a) and 1(b), respectively, on a regular square mesh corresponding to an angular spacing of  $0.7^\circ$ . The sampling density of EDC's is significantly higher in regions of  $\mathbf{k}$  space where the intensity is high, and sparse in regions corresponding to unoccupied states. Our angular resolution, as defined by the acceptance cone of the spectrometer, is shown as the circle centered on  $S$ . Unlike the work of Aebi *et al.*, on Bi2212, our effective windowing function in this plot is simply the Gaussian instrument response rather than a square window convolved with the instrument response.

The orthorhombic symmetry breaking of the chains is immediately clear in both orientations, with the intensity at  $E_F$  dominated by weight from the narrow spectral feature at  $Y$ ,

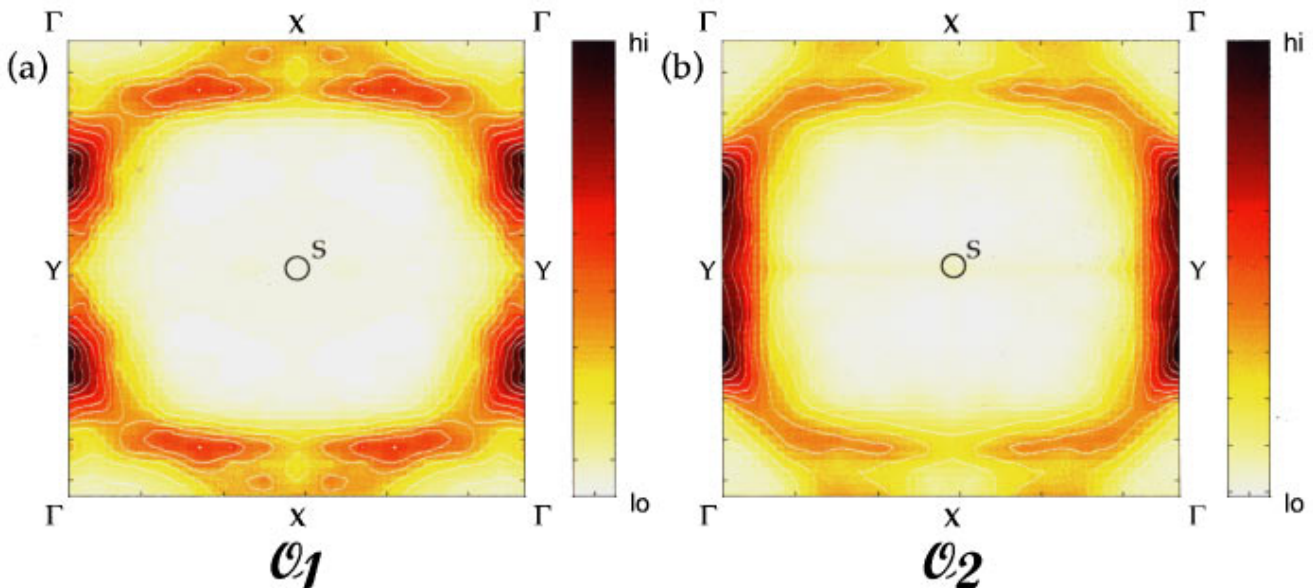


FIG. 4. (Color) Photoemission intensity maps at the Fermi energy for  $\mathcal{O}_1$  ( $\mathbf{E}||\Gamma S$ ), and  $\mathcal{O}_2$  ( $\mathbf{E}||\Gamma Y$ ) are shown in panels (a) and (b), respectively. Data taken in the  $\Gamma XSY$  quadrant have been reflected along symmetry axes to produce a map of the entire irreducible Brillouin zone. The black circle at the center indicates the angular acceptance cone of the spectrometer.

although to a lesser degree in  $\mathcal{O}_1$  than in  $\mathcal{O}_2$ . The highest intensities, found along  $\Gamma Y$ , correspond to the oft-discussed “extended van Hove singularity” (evHs) in Y123.<sup>22–24</sup> This feature appears *only* along  $\Gamma Y$  in our untwinned samples, unlike twinned crystals where the  $\Gamma X$  and  $\Gamma Y$  lines are degenerate, and disappears for polarization perpendicular to the  $\text{CuO}_3$  chains, indicating that the evHs is actually a chain-related feature of the electronic structure stemming from the surface termination of the cleaved crystals. An extensive discussion of arguments in support of this attribution is presented in the preceding companion paper.<sup>18</sup>

The fourfold symmetric signal originating in the  $\text{CuO}_2$  planes dominates emission from the bulk chains, which should form a Fermi-surface sheet parallel to  $\Gamma X$ , presumably due to the surface sensitivity of the photoemission technique. Overall the measured intensity contours are qualitatively consistent with those observed in photoemission studies of other high- $T_c$  materials, both hole and electron doped,<sup>3–5,25–27</sup> which are found to have a large hole pocket centered on  $(\pi, \pi)$ . Interestingly, the small “stick” Fermi-surface pocket predicted to be centered on the  $S$  point in LDA calculations is entirely absent in our data, contrasting with earlier measurements.<sup>2</sup> The fact that the bands responsible for this pocket arise largely from hybridization of Ba and apical O(4) atoms makes it plausible that the BaO surface termination may strongly perturb them from their bulk energies, and consequently affect their Fermi crossing behavior.<sup>28</sup>

Qualitatively both intensity maps bear a strong resemblance to the LMT0 Fermi surfaces, with the exception of the absent “stick” pocket. The apparent width of the Fermi-surface segments is roughly twice the experimental angular resolution, becoming even larger near the  $X$  point, where it is limited by the spectrometer energy rather than  $\mathbf{k}$  resolution in these regions where the bands are quite flat. In  $\mathcal{O}_1$  a large pocket centered on  $S$  is seen along with significant weight distributed near  $X$ , while  $\mathcal{O}_2$  shows a similar pocket and additional weight bifurcated away from  $X$  along the  $\Gamma X$  direction. Neither geometry shows strong evidence for a chain Fermi-surface crossing along  $\Gamma Y$ , although weight arising from the surface state appears where it would be expected, in the region where chain states lie in the unoccupied bands.<sup>29</sup> Because of the breadth of the features in panels 4(a) and 4(b), the data are consistent with both the  $pd\sigma^*$  antibonding and  $pd\sigma$  bonding plane pockets but the two may not be clearly distinguished except possibly near  $X$ . Unfortunately the weight near  $X$  may arise from either the saddle-point bifurcation of the antibonding pocket induced by plane dimpling, or from the chain sheet which manifests significant  $c$ -axis dispersion in this part of the zone due to hybridization with the  $pd\sigma^*$  states. Because the value of  $k_z$  is not well defined in our measurements, it is likely that our data will include contributions from values of  $k_z$  where stationary initial states lead to density of states enhancement. We note that the data from the  $\Gamma X\Gamma$  octant is qualitatively similar to the earlier Fermi-surface measurement of twinned Y123 by Liu *et al.*,<sup>3</sup> taken in the  $\mathcal{O}_2$  geometry with 21 eV photons from a He gas discharge lamp.

To identify Fermi-surface segments and crossing points more precisely, we have looked at  $I(E_F)$  contours along

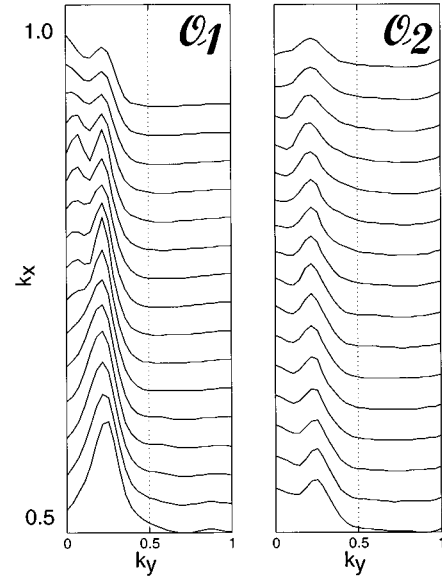


FIG. 5. Normalized cuts through the data of Figs. 4(a) and 4(b) parallel to  $\Gamma Y$  for  $k_x$  ranging between 0.5 and 1.0. Two peaks corresponding to two separate Fermi-surface crossings appear in the data in both sample geometries.

lines paralleling both  $\Gamma Y$  and  $\Gamma X$  for various values of  $k_x$  and  $k_y$ , respectively. In this approach, which is complementary to band-structure identification, with a peak being identified in  $\mathbf{k}$  for fixed  $\omega = E_F$ , Fermi-surface crossings should appear as peaks in the intensity as a function of  $\mathbf{k}$ . Figure 5 shows normalized Fermi level intensity curves for cuts parallel to  $\Gamma Y$  for  $k_x$  between 0.5 and 1.0, corresponding to cross-sectional slices of the data in Figs. 4(a) and 4(b). The data in both plots have a double-peaked structure extending over a large fraction of the  $\Gamma X$  line, with a smaller feature near the  $k_y = 0$  line and a more prominent one around  $k_y = 0.2$  which merge into a single broader peak nearer to  $\Gamma$  in  $\mathcal{O}_1$ , but remain distinct in  $\mathcal{O}_2$ . An important technical detail which arises when performing such an analysis is the occurrence of spurious peaks when the line along which  $I(E_F)$  is being interpolated lies parallel (or nearly so) to a segment of the Fermi surface. In this case, the actual Fermi “crossing” will be extremely broad, and noise in the data may give rise to features which do not correspond to the true Fermi surface. For this reason, data from these regions must be disregarded as unreliable.

Application of the gradient method to the data of Fig. 4 is presented in Figs. 6(a) and 6(b). Sample lifetime constraints and data acquisition time make it impossible to acquire an arbitrarily dense set of EDC’s, necessitating interpolation of our data in  $\mathbf{k}$  space to generate a uniform mesh which is then numerically smoothed by convolution with a two-dimensional window function having a breadth 1.5 times the instrument width, and differentiated to form the quantity  $|\nabla_{\mathbf{k}} \ln n(\mathbf{k})|$ .<sup>30</sup> In choosing grids spanning the Brillouin zone (see Fig. 1), we were guided by previous investigations, allowing us to concentrate spectra in regions where there is appreciable spectral weight below  $E_F$ , and sample the regions containing unoccupied states more sparsely. The logarithmic gradient was chosen to minimize the intensity varia-

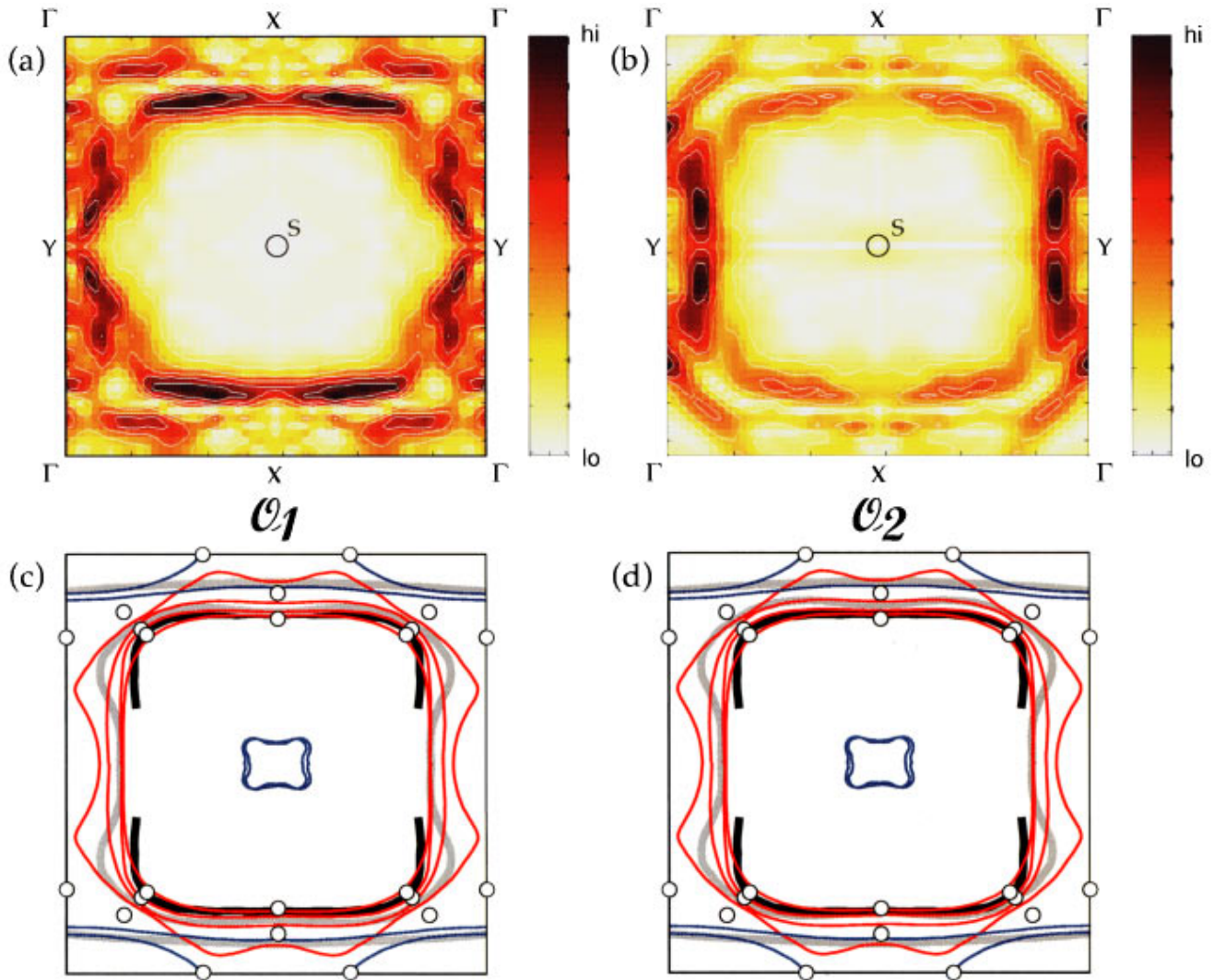


FIG. 6. (Color) Fermi surfaces determined from the logarithmic gradient of the photoemission intensity at the Fermi energy, plotted as in Fig. 4. The small segments near  $\Gamma$  are artifacts due to the small effective window of  $\omega$  integration. Panels (c) and (d) show the Fermi surfaces derived from the data (thick black and gray lines) along with Fermi-surface crossings identified by conventional band dispersion measurements (open circles) (Ref. 18). Superimposed are the LMTO calculated Fermi surfaces for  $k_z=0, \pi$  (plane states are shown in red, chains in blue).

tions seen over the BZ in the raw data; other than diminished contrast, the results of application of the bare gradient are essentially indistinguishable.

Examination of Figs. 6(a) and 6(b) reveals the expected large hole pocket centered on  $S$ , with significantly narrower Fermi sections than observed in the photoemission intensity maps. In contrast with the photoemission intensity maps discussed above, the segments resolved with the gradient are comparable in width to the instrumental  $\mathbf{k}$  resolution defined by our angular aperture (broadened by smoothing). We verified from the band dispersions that the parallel segments near the  $\Gamma$  point result from the finite energy window, with a quasiparticle dispersing up from higher binding energy passing first through the lower edge of the energy window, then crossing the Fermi surface, as discussed in Sec. II. The remaining portions are sections of the true Fermi surface, although segments in the vicinity of the surface peak at  $Y$  are aliased by the spurious spectral weight of this feature and are not representative of the bulk Fermi surface.

In both orientations we can clearly resolve the strongly

nested inner (bonding) plane FS pocket, with weak indications of the outer (antibonding) pocket visible primarily near  $X$  and  $Y$ . While the derivative data is too noisy to unambiguously reveal both crossings along  $\Gamma S$ , detailed analysis of dispersion relations along this line clearly demonstrates their presence.<sup>18</sup> The chain band is weakly apparent, though it presumably overlaps to a large degree with the antibonding plane segments around  $X$ . Figures 6(c) and 6(d) show subjective Fermi surfaces, determined from the plots in 6(a) and 6(b), as thick lines. Superimposed are LMTO Fermi-surface contours for  $k_z=0, \pi$ , with the plane bands in red and chains in blue. Experimental FS crossings determined from band dispersions using the conventional method are indicated by the open circles.<sup>18</sup> The expected bifurcated saddle points in the antibonding Fermi surface may be resolved in segments paralleling  $\Gamma Y$ , indicated by the thick gray lines. Our ability to make quantitative statements about this region of the Brillouin zone is, however, compromised by the large contribution of the surface peak near  $Y$ . A complimentary bifurcation of the saddle point in the  $\Gamma X$  direction, if present, is not well

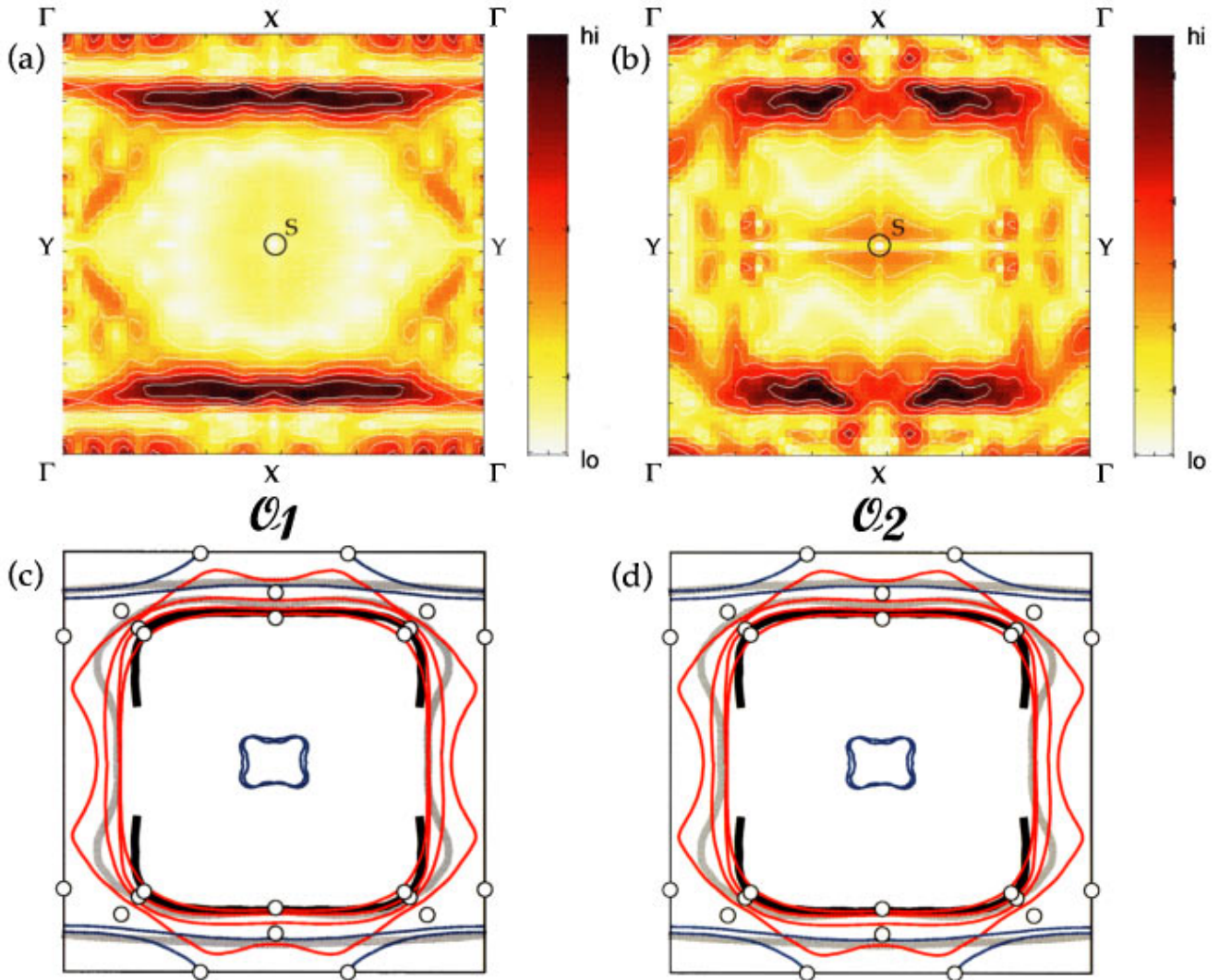


FIG. 7. (Color) Fermi surfaces determined from the logarithmic gradient of the integrated photoemission intensity, plotted as in Fig. 4. The  $\omega$ -integration cutoff of 0.6 eV was chosen to encompass all quasiparticles seen in the ARPES EDC's which disperse through the Fermi level.

resolved, in contrast with LDA predictions. This is likely a consequence of strong  $c$ -axis dispersion distributing spectral weight over a larger region of  $\mathbf{k}$  space for the dispersive  $p d \sigma^*$  FS sheets in this part of the Brillouin zone. In  $\mathcal{O}_2$ , where  $\mathbf{E}$  is parallel to the  $\text{CuO}_3$  chains, we note that even using the logarithmic gradient technique the emission from the feature near  $Y$  is by far the most prominent contribution, while the relative contributions are comparable in  $\mathcal{O}_1$ .

The results of the gradient method applied to  $n(\mathbf{k})$  data integrated over the observable quasiparticle bandwidth of roughly 0.6 eV are shown in Figs. 7(a) and 7(b). The most dramatic difference between these plots and those in Figs. 4 and 6 is the significant enhancement of the cross section for Fermi-surface weight along  $\Gamma X$  in both geometries, and a simultaneous suppression of the weight near  $Y$ . A nonnegligible contribution from the bulk chain Fermi surface is also resolved along  $\Gamma Y$  near the  $\Gamma$  point in panel 7(a). Its absence in panel 7(b) is likely the result of weight enhancement of the surface feature along this line in  $\mathcal{O}_2$ . Another notable difference is the width of the segments, which is measurably greater than the expected resolution in both panels, contrast-

ing with Fig. 6; we attribute this to unresolved overlap of the two-plane Fermi surfaces and/or the chain FS. Finally, unlike the preceding figures, there also appears to be a weakly resolved pocket centered at  $S$  in these plots which might be attributed to the otherwise unobserved “stick” sheet. However, close examination of the band dispersions reveals that these are actually artifacts from a downward dispersing band which has its maximum at the  $S$  point, with a binding energy slightly lower than the upper limit for our  $\omega$  integration. For this reason, it is important to consider all aspects of the photoemission data in a unified manner.

Comparison of the results of the simple intensity mapping [Figs. 4(a) and 4(b)] with the results of application of the momentum space derivative method (Figs. 6 and 7) emphasizes some of the pitfalls of naively applying the photoelectron diffraction method to the problem of Fermi-surface measurement. While the derivative data shows excellent overall agreement with data points obtained subjectively from the band dispersions as well as with the LDA predictions, the “Fermi surfaces” obtained directly from the intensity maps are both much broader and larger in volume. This

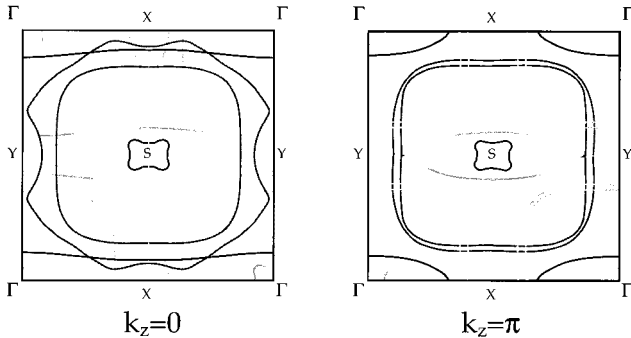


FIG. 8. “Shadow band” Fermi surfaces generated from the LMTO calculations of Fig. 3. Sheets for each value of  $k_z$  are shifted by  $(\pi, \pi)$  relative to the Fermi surface for the primitive unit cell to reflect incipient antiferromagnetic order. Such ordering will, in the static limit, lead to a Fermi surface of half the original volume, rotated by  $45^\circ$ , in which  $\Gamma$  and  $S$  are degenerate.

observation again underscores the importance of retaining the full information contained in the photoemission EDC’s for consistent identification of Fermi surfaces. Future development of the momentum space technique with more specialized equipment should improve the noise level in derivative data, and, by further exploitation of polarization dependence, may be able to more clearly discriminate the Fermi-surface contributions from the planes and chains.

#### IV. SHADOW BANDS IN Y123

The shadow bands observed in the Fermi surface of Bi2212 by Aebi *et al.*, seen in normal-state measurements of the photoemission intensity at room temperature, were attributed to echoes of the bonding FS shifted by  $(\pi, \pi)$  arising from strong antiferromagnetic correlations. This interpretation has been controversial; the appearance of these features in their experiment is particularly surprising because the data were taken on optimally doped, metallic Bi2212 at 300 K, which has an extremely short antiferromagnetic correlation length on the order of a planar lattice constant. A possible alternative explanation of this effect is a weak  $c(2 \times 2)$  structural distortion which would mimic the effects of static antiferromagnetic order. Our data on Y123, which were taken at low temperature (20 K), provide an independent test of this hypothesis on a material known to be free of such structural distortions.

Figure 8 shows schematically what would be expected in the case of Y123 if antiferromagnetic long-range order were present; the true LMTO FS is indicated by the solid lines, while the shifted echoes plotted in gray represent the folding from the AF potential. One should be able to directly observe these echoes in the photoemission data experimentally, with the most prominent features of the unperturbed Fermi surface presumably having the strongest shadows as well. Examination of the experimental Fermi surfaces in Figs. 4, 6, and 7 does not reveal any indication of such a folding in any of our data. In addition, close inspection of EDC’s along the  $\Gamma S$  line shows no evidence for the presence of a peak shifted by  $(2\pi/3, 2\pi/3)$  corresponding to the main Fermi-surface crossing near  $(\pi/3, \pi/3)$ .<sup>18</sup> This data suggests that the

shadow bands seen in Bi2212 are structural in origin, and do not arise from the vestigial antiferromagnetic order in this material, and are consistent with earlier investigations searching for closed pockets along  $\Gamma S$  in twinned Y123.<sup>3</sup>

#### V. SUMMARY AND CONCLUSIONS

In summary, we have discussed several techniques for extraction of Fermi surfaces from angle-resolved photoemission data, comparing and contrasting their merits and disadvantages. A method of quantitative Fermi-surface determination based on a momentum space DOS analysis is proposed which eliminates many of the uncertainties of the other techniques and is demonstrated to provide results consistent with those approaches. Various different methods have been applied to sets of ARPES spectra taken on untwinned crystals of optimally doped Y123 in inequivalent photon polarization geometries and the results compared and interpreted within the context of *ab initio* LMTO calculations of the Fermi surface of this material.

Our data unambiguously reveal a strongly nested inner Fermi-surface pocket centered on  $S$  which we attribute to the  $\text{CuO}_2$  bonding  $pd\sigma$  bands. The bilayer splitting of the plane bands, which is clearly resolved in the polarization-dependent energy distribution curves presented in the companion paper,<sup>18</sup> appears as a more weakly resolved outer sheet in the  $\mathbf{k}$ -space data. We also resolve vestiges of the principal chain sheet in some of the data, but it is significantly suppressed, consistent with a strongly modified surface chain termination. While the absence of bilayer splitting in this material would be a striking manifestation of non-Fermi-liquid behavior, the presence of such splitting is not necessarily incompatible with Luttinger-liquid concepts since these effects should manifest themselves at much lower energy scales. Our data show no sign of the stick Fermi surface centered at  $S$ , consistent with previous measurements. We also have considered the evidence in our experiments for antiferromagnetic shadow Fermi surfaces, and compared our results with those from Bi2212. Unlike Bi2212, we find no evidence for the presence of such shadow bands in any of our data on optimally doped Y123.

#### ACKNOWLEDGMENTS

The data in this study were obtained at the Stanford Synchrotron Radiation Laboratory (SSRL) which is operated by the DOE Office of Basic Energy Sciences, Division of Chemical Sciences. The Office’s Division of Materials Science has also provided support for this study. The Stanford work was supported through ONR Grant No. 00014-95-1-0960, and the Center for Materials Research. D.A.B., R.L., and W.N.H. acknowledge the support of the Natural Science and Engineering Research Council of Canada, and the Canadian Institute for Advanced Research. M.C.S. would like to express his gratitude to Professor Ole Andersen for the opportunity to work at the Max-Planck-Institut, Stuttgart, and would also like to thank Dr. Ove Jepsen, Dr. Sasha Liechtenstein, and Dr. Warren Pickett for stimulating discussions and Dr. Armin Burkhardt for assistance with visualization. M.C.S. gratefully acknowledges the support of the Fannie and John Hertz Foundation.

- <sup>1</sup>C. G. Olson, R. Liu, A.-B. Yang, D. W. Lynch, A. J. Arko, R. S. List, B. W. Veal, Y. C. Chang, P. Z. Jiang, and A. P. Paulikas, *Science* **245**, 731 (1989).
- <sup>2</sup>J. C. Campuzano, G. Jennings, M. Faiz, L. Beaulaigue, B. W. Veal, J. Z. Liu, A. P. Paulikas, K. Vandervoort, H. Claus, R. S. List, A. J. Arko, and R. J. Bartlett, *Phys. Rev. Lett.* **64**, 2308 (1990).
- <sup>3</sup>R. Liu, B. W. Veal, A. P. Paulikas, J. W. Downey, P. J. Kostić, S. Fleshler, U. Welp, C. G. Olson, X. Wu, A. J. Arko, and J. J. Joyce, *Phys. Rev. B* **46**, 11 056 (1992).
- <sup>4</sup>D. M. King, Z.-X. Shen, D. S. Dessau, B. O. Wells, W. E. Spicer, A. J. Arko, D. S. Marshall, J. DiCarlo, A. G. Loeser, C.-H. Park, E. R. Ratner, J. L. Peng, Z. Y. Li, and R. L. Greene, *Phys. Rev. Lett.* **70**, 3159 (1993).
- <sup>5</sup>D. S. Dessau, Z.-X. Shen, D. M. King, D. S. Marshall, L. W. Lombardo, P. H. Dickinson, J. DiCarlo, A. G. Loeser, C.-H. Park, A. Kapitulnik, and W. E. Spicer, *Phys. Rev. Lett.* **71**, 2781 (1993).
- <sup>6</sup>A. Santoni, L. J. Terminello, F. J. Himpsel, and T. Takahashi, *Appl. Phys. A: Solids Surf.* **52**, 299 (1991).
- <sup>7</sup>P. Aebi, J. Osterwalder, P. Schwaller, L. Schlapbach, M. Shimoda, T. Mochiku, and K. Kadowaki, *Phys. Rev. Lett.* **72**, 2757 (1994).
- <sup>8</sup>M. Randeria, H. Ding, J.-C. Campuzano, A. Bellman, G. Jennings, T. Yokoya, T. Takahashi, H. Katayama-Yoshida, T. Mochiku, and K. Kadowaki, *Phys. Rev. Lett.* **74**, 4951 (1995).
- <sup>9</sup>Th. Straub, R. Claessen, P. Steiner, V. Eyert, K. Friemelt, E. Bucher, and S. Hüfner (unpublished).
- <sup>10</sup>H. Ding, A. F. Bellman, J.-C. Campuzano, M. Randeria, M. R. Norman, T. Yokoya, T. Takahashi, H. Katayama-Yoshida, T. Mochiku, K. Kadowaki, G. Jennings, and G. P. Brivio, *Phys. Rev. Lett.* **76**, 1533 (1996).
- <sup>11</sup>W. E. Pickett, R. E. Cohen, and H. Krakauer, *Phys. Rev. B* **42**, 8764 (1990).
- <sup>12</sup>O. K. Andersen, A. I. Liechtenstein, C. O. Rodriguez, I. I. Mazin, O. Jepsen, V. P. Antropov, O. Gunnarsson, and S. Gopalan, *Physica C* **185-189**, 147 (1991).
- <sup>13</sup>O. K. Andersen, O. Jepsen, A. I. Liechtenstein, and I. I. Mazin, *Phys. Rev. B* **49**, 4145 (1994).
- <sup>14</sup>J. G. Tobin, C. G. Olson, C. Gu, J. Z. Liu, F. R. Solal, M. J. Fluss, R. H. Howell, J. C. O'Brien, H. B. Radousky, and P. A. Sterne, *Phys. Rev. B* **45**, 5563 (1992).
- <sup>15</sup>J. Osterwalder, P. Aebi, P. Schwaller, L. Schlapbach, M. Shimoda, T. Mochiku, and K. Kadowaki, *Appl. Phys. A: Solids Surf.* **60**, 247 (1995).
- <sup>16</sup>D. J. Singh and W. E. Pickett, *Phys. Rev. B* **51**, 3128 (1995).
- <sup>17</sup>S. Chakravarty, *Phys. Rev. Lett.* **74**, 1885 (1995).
- <sup>18</sup>M. C. Schabel *et al.*, preceding paper, *Phys. Rev. B* **57**, 6090 (1998).
- <sup>19</sup>P. Aebi, T. J. Kreutz, J. Osterwalder, R. Fasel, P. Schwaller, and L. Schlapbach, *Phys. Rev. Lett.* **76**, 1150 (1996).
- <sup>20</sup>J. Osterwalder, T. Greber, P. Aebi, R. Fasel, and L. Schlapbach, *Phys. Rev. B* **53**, 10 209 (1996).
- <sup>21</sup>S. Chakravarty, A. Sudbø, P. W. Anderson, and S. Strong, *Science* **261**, 337 (1993).
- <sup>22</sup>K. Gofron, J. C. Campuzano, H. Ding, C. Gu, R. Liu, B. Dabrowski, B. W. Veal, W. Cramer, and G. Jennings, *J. Phys. Chem. Solids* **54**, 1193 (1993).
- <sup>23</sup>K. Gofron, J. C. Campuzano, A. A. Abrikosov, M. Lindroos, A. Bansil, H. Ding, D. Koelling, and B. Dabrowski, *Phys. Rev. Lett.* **73**, 3302 (1994).
- <sup>24</sup>B. W. Veal and C. Gu, *J. Electron Spectrosc. Relat. Phenom.* **66**, 321 (1994).
- <sup>25</sup>Z.-X. Shen, D. S. Dessau, B. O. Wells, D. M. King, W. E. Spicer, A. J. Arko, D. Marshall, L. W. Lombardo, A. Kapitulnik, P. Dickinson, S. Doniach, J. DiCarlo, A. G. Loeser, and C.-H. Park, *Phys. Rev. Lett.* **70**, 1553 (1993).
- <sup>26</sup>Z.-X. Shen and D. S. Dessau, *Phys. Rep.* **253**, 2 (1995).
- <sup>27</sup>R. O. Anderson, C. G. Olson, J. W. Allen, C. Janowitz, L. Z. Liu, J.-H. Park, M. B. Maple, Y. Dalichaouch, M. C. De Andrade, and M. Jardim, *Phys. Rev. Lett.* **70**, 3163 (1993).
- <sup>28</sup>I. I. Mazin, O. Jepsen, O. K. Andersen, A. I. Liechtenstein, S. N. Rashkeev, and Y. A. Uspenskii, *Phys. Rev. B* **45**, 5103 (1992).
- <sup>29</sup>S. Hüfner, *Photoelectron Spectroscopy* (Springer, Berlin, 1995), Chap. 8.
- <sup>30</sup>*MATLAB Reference Guide* (MathWorks, Natick, MA).